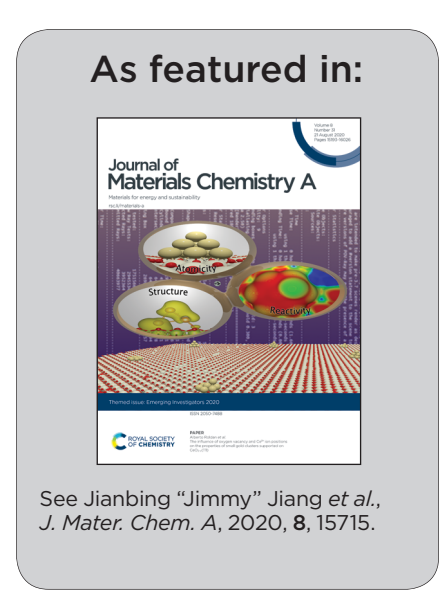


Proposing a non-aqueous redox flow battery based on all-PEGylated redox-active metal-free organic molecules by a group of researchers led by Dr Jiang from University of Cincinnati.

All-PEGylated redox-active metal-free organic molecules in non-aqueous redox flow battery

A NAORFB with all-PEGylated, metal-free organic compounds as electroactive materials is demonstrated. PEGylated phenothiazine and PEGylated viologen are utilized as the catholyte and anolyte, respectively. Combined with a composite nanoporous aramid nanofiber separator, the all-PEGylated NAORFB presents outstanding cyclability, with a capacity retention of 99.90% per cycle and average Coulombic efficiency of 99.7%, superior to the NAORFBs using half-PEGylated and non-PEGylated electrolytes.





Journal of Materials Chemistry A



PAPER

View Article Online
View Journal | View Issue



Cite this: J. Mater. Chem. A, 2020, 8, 15715

Received 26th February 2020 Accepted 17th March 2020

DOI: 10.1039/d0ta02303e

rsc li/materials-a

All-PEGylated redox-active metal-free organic molecules in non-aqueous redox flow battery†

Jingchao Chai, Amir Lashgari, Xiao Wang, Caroline K. Williams and Jianbing "Jimmy" Jiang **

Non-aqueous organic material-based redox flow batteries (NAORFBs) possess the advantage of using organic solvents to achieve high electrochemical potential. However, regardless of the great progress made in this regard in the past decade, further development has been restricted by the lack of stable electroactive organic materials and highly selective separators. Here, we present a NAORFB with all-PEGylated, metal-free, organic compounds as electroactive materials. PEGylated phenothiazine and PEGylated viologen are utilized as the catholyte and anolyte, respectively. Combined with a composite nanoporous aramid nanofiber separator, the all-PEGylated NAORFB presents outstanding cyclability, with a capacity retention of 99.90% per cycle and average coulombic efficiency of 99.7%. By contrast, NAORFBs using half-PEGylated and non-PEGylated electrolytes display inferior cyclability owing to the crossover of non-PEGylated materials. An extended investigation was also performed on the batteries using non-PEGylated or half-PEGylated materials for mechanistic elucidation. This work validates the PEGylation strategy in NAORFBs for enhanced overall performance with respect to solubility, cyclability, and alleviated crossover.

Introduction

Over the past century, there has been a significant increase in demand for electricity. The continually increasing content of greenhouse gases generated from traditional fossil fuels has prompted researchers worldwide to develop clean energy, such as wind and solar energy. 1-3 However, the intrinsic intermittence and fluctuation of these renewable energy sources pose serious challenges. Energy storage devices, such as lithium (metal),4-12 sodium,13,14 aluminum,15 and magnesium ion batteries, 16,17 have played an important role in reducing peak shaving and valley filling in electric networks. Among the emerging energy storage devices, redox flow batteries (RFBs) have attracted much attention.18-21 RFBs store energy in liquid electrolyte reservoirs, which decouple the energy and power densities.22-25 Non-aqueous organic material-based redox flow batteries (NAORFBs) have been studied in recent years owing to their wide electrochemical window of non-aqueous electrolytes and vast molecular diversity.²⁶⁻³⁸ However, a limiting factor that retards further development of the NAORFBs is the crossover of electroactive compounds through the membrane into the opposite compartments, causing inferior cyclability performance.26,39,40 The crossover issue is less severe in the

conventional aqueous RFBs because of the availability of ionexchange membranes, such as the commercially available and widely used Nafion®, Fumasep®, AMV®, and DSV® membranes,20,41-48 which can suppress the permeability of redox-active species. These ion-exchange membranes usually possess super-high ionic conductivity (>100 mS cm⁻¹) in aqueous electrolytes,48-50 endowing the aqueous RFBs with superior power densities. Unfortunately, merely using these membranes in non-aqueous electrolytes typically induces new issues, such as inferior stability and high resistance (<100 mS cm⁻¹),^{27,51-53} resulting in low charge/discharge rate and power density. The pretreatment of Nafion® membranes to convert the proton of the sulfonic acid to lithium ion52 or tetraalkylammonium,54 such as tetrabutylammonium or tetraethylammonium, does not substantially improve the performance. Size exclusion-based porous membranes, such as Daramic® and Celgard® membranes, have been used in some non-aqueous symmetrical batteries or catholyte-anolyte-mixed batteries, but typically in low coulombic efficiencies (80-95%)31,39,40,55-60 and high self-discharge rates, owing to the large pore sizes (20-200 nm). NAORFBs using inorganic glass ceramic separators display high coulombic efficiencies and high charge/ discharge current density.29,61 However, their intrinsic brittleness and high cost prevent their wide application.

Two strategies can be adopted to address the aforementioned issues and improve the overall battery performance. One is to increase the molecular size of electroactive compounds to suppress penetration through the membrane based on

Department of Chemistry, University of Cincinnati, P.O. Box 210172, Cincinnati, Ohio 45221-0172, USA. E-mail: jianbing.jiang@uc.edu

 $[\]dagger$ Electronic supplementary information (ESI) available: Synthesis of compounds, NMR spectra, photographs of compounds, CV, battery performances. See DOI: 10.1039/d0ta02303e

a physical blocking mechanism. For example, small electroactive compounds can be incorporated on redox-innocent polymer backbones^{24,57,62,63} or decorated with long tails.^{23,64,65} The second strategy is to design novel membranes with high ion selectivity, low resistance, and high solvent compatability.^{26,66} The porous membrane can be modified with positively or negatively charged ions to introduce ion-exchange features,⁶⁶⁻⁶⁹ thus suppressing crossover by a combination of steric hindrance and Donnan exclusion mechanism.^{53,70} The Sanford group reported a Fumasep® anion exchange membrane to separate the positively charged anolyte and catholyte.⁶⁷⁻⁶⁹ Both strategies (molecular engineering and membrane decoration) are used in a synergistic manner to improve the overall battery performance.

Several types of organic redox-active materials have been reported in NAORFBs, including (but not limited to): (1) viologens. The most promising feature of using viologens as the analyte is the two-electron redox activity for higher energy capacity compared to its one-electron-active peers. In comparison to the intrinsically water-soluble viologens, 19,49,71,72 Liu et al. reported a highly organic soluble viologen by replacing its halogen anions with less polar bis(trifluoromethanesulfonyl)imide (TFSI) units and successfully applied it in NAORFB;30 (2) ferrocene (Fc). As a highly electrochemically stable organometallic complex, Fc is commonly used as a catholyte in NAORFBs. 29,73 However, the low redox potential of Fc (0.69 V vs. standard hydrogen electrode) does not take full advantage of the wide electrochemical window of non-aqueous solvents. In addition, the energy density of Fc is relatively low owing to the limited solubility in organic solvents [200 mM in acetonitrile (ACN), and even lower in carbonate solvents].38,74 Derivatized Fc, such as quaternized ferrocene30,38,75 and brominated ferrocene,73 were also developed to improve the solubility and/or increase the redox potential; and (3) phenothiazine (PTZ). As catholyte materials, 44,57,76,77 PTZs can undergo facile molecular modification on the N atom and aromatic ring to optimize solubility, stability, and redox potentials, making PTZs attractive in NAORFBs.77 For practical applications, an electroactive compound in RFB should possess features including (1) high electrolyte stability, (2) wide electrochemical window, (3) high electrolyte solubility, and (4) mitigated crossover (Fig. 1). Few (if any) materials satisfy all four criteria.

Recently, we investigated a PEGylated strategy and used PEGylated viologens as anolytes for the demonstration of proof-

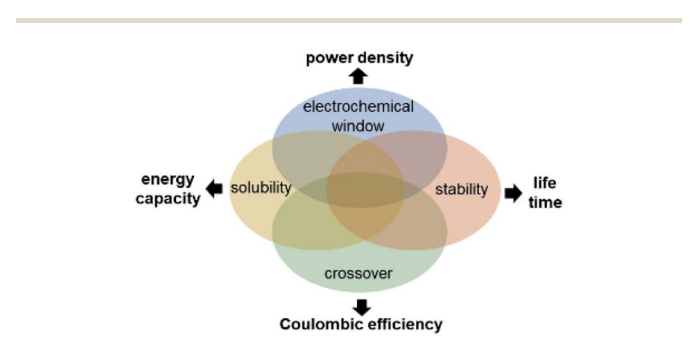


Fig. 1 Venn diagram depicting the four key requirements for redoxactive species in NAORFBs.

of-concept in the NAORFB.64 The introduction of poly(ethylene glycol) (PEG) increased the molecular size of viologen and improved solubility in all the charged and discharged states of viologen in the organic solvent. In this paper, we present a PEGylated PTZ as the catholyte. PEGylated electroactive materials have been applied in NAORFBs.23,58 However, the majority of the reported materials employed lower degree of PEG units with limited capability for crossover suppression. The PEGylated viologen and PEGylated phenothiazine herein possess lower permeability due to the increases molecular size by the introduction of higher degree of PEG chains. Paired with the PEGylated viologen, the all-PEGylated battery exhibited substantially long cyclability. An extended investigation was also conducted on the NAORFBs using partially or non-PEGylated compounds and illustrated that the all-PEGylated system possesses superior cyclability and higher coulombic efficiency. This study validates that the PEGylation strategy can greatly improve the performance of redox-active materials in NAORFBs.

Experimental section

Materials

Sodium hydride, phenothiazine, sodium sulfate, potassium hydroxide, 1-iodopropane, anhydrous acetonitrile (99.8%), and tetrabutylammonium hexafluorophosphate were purchased from Sigma-Aldrich. Methylene dichloride and N,N-dimethylformamide were obtained from Fisher Chemical. Dimethyl sulfoxide was purchased from TCI Chemicals. The aramid nanofiber was purchased from the Thread Exchange. The Daramic separator was provided by Daramic LLC. Tetrabutylammonium hexafluorophosphate (TBAPF₆) was recrystallized in absolute ethanol and dried in vacuo. The other materials were used as purchased without any purification. The ¹H NMR and ¹³C NMR analyses were performed at room temperature using a Bruker AV 400 MHz spectrometer. Chemical shifts are based on the ppm unit. Electrospray ionization-mass spectrometry (ESI-MS) analysis was performed on an Orbitrap Fusion Lumos mass spectrometer from Thermo Scientific. Compounds PEGylated viologen (PEG12-V, with 12 oxyethylene units),64 methyl viologen (Me-V)30,78 and N-propyl phenothiazine (C3-PTZ)⁷⁹ were prepared according to reported procedures.

Electrochemical measurement

All the cyclic voltammetry (CV) tests were conducted in 0.1 M TBAPF₆-ACN solution in an argon-filled glovebox. The CV studies were carried on a Bio-Logic potentiostat. For a CV study, a glassy carbon (3 mm in diameter) and a Pt wire electrode were used as the working and counter electrode, respectively. Ag/AgNO₃ electrode with 0.01 M AgNO₃/ACN solution was used as reference electrode.

Linear sweep voltammetry (LSV) studies were carried out using a Pine modulated speed rotator with CHI760e electrochemical workstation. Rotating disk electrode (RDE, diameter: 5 mm), Pt wire electrode and Ag/AgNO₃ electrode were used as the working, counter and reference electrodes, respectively.

Before testing, the samples were purged with argon for 10 min to remove the dioxygen. LSV dates were collected at different rotation rates from 100 to 2500 rpm. Diffusion coefficient (D) of electroactive material was calculated from Levich plot:46,48,80

$$i = 0.620 nFA C_0 D^{2/3} \omega^{1/2} v^{-1/6}$$

where i is limiting current density (A), n is the number of electrons in redox process, F is Faraday's constant (96 485 C mol^{-1}), A is the area of the glassy carbon electrode (0.196 cm²), C_0 is the concentration of active material (1 \times 10⁻⁶ mol cm⁻³), D is the diffusion coefficient (cm² s⁻¹), ω is angular rotation rate (rad s^{-1}), and v is the kinematic viscosity of 0.1 M TBAPF₆-ACN $(0.00442 \text{ cm}^2 \text{ s}^{-1}).$

The mass-transfer-independent kinetic current i_k was obtained from the Koutecký-Levich plot for different overpotentials (the reciprocal of the current at overpotentials vs. the reciprocal of the square root of the rotation rate).20,62 Exchange current i_0 can be obtained from the Butler-Volmer equation^{41,62} viaa Tafel plot [log($i_{\rm k})vs.$ overpotential], which yields the kinetic oxidation rate constant k_0 (cm s⁻¹) from following equation:

$$i_0 = FAk_0C_0$$

The transfer coefficient (α) was obtained from Tafel analysis:

Tafel slope =
$$(1 - \alpha)F/(2.3RT)$$

where R is the universal gas constant $(8.314 \text{ J (K mol)}^{-1})$ and T is the absolute temperature (298 K).

Permeability measurement

The permeability measurements of active materials were carried out following the procedures in the ref. 20 and 64. The samples of 15 mL 50 mM active material in 0.1 M TBAPF₆-ACN were added to one side of the H-cells. The blank electrolyte solution without redox-active materials was used in the other side. The H-cell was separated by composite nanoporous aramid nanofiber (CANF) membrane. The concentrations of active materials were calculated from the calibration curve of the peak current density vs. concentration. The permeability (P) is calculated from the following equation:20

$$P = \frac{\ln\left(1 - \frac{2C_{\rm r}}{C_0}\right)\left(-\frac{Vl}{2A}\right)}{t}$$

where $C_{\rm r}$ is the concentration measured at the receiving side (mol cm $^{-3}$), C_0 is the active species concentration in the working chambers (mol cm $^{-3}$), V is the volume (cm 3), l is the membrane thickness (cm), A is the membrane area (cm 2), and t is the test time (s).

DFT calculation

All calculations were carried out by using Gaussian 09 software for original and one-electron oxidation state.81 All oxidation states were optimized at ground states with M06-2x functional:

Minnesota '06 2x global hybrid functional with 54% Hartree-Fock exchange and 6-31+G(d) basis sets. The universal solvation model SMD was selected to optimize all geometries in ACN to include the solvation effect to the free energies. The molecular orbitals (MOs) and molar volume calculations were carried out at M06-2x/6-31+G(d) level.

Battery measurement

The flow battery possesses an active area of 28 cm², and is composed of a metal plate, polytetrafluoroethylene plate, copper plate, graphite current collector, polytetrafluoroethylene frame, and graphite-felt electrodes. The CANF membrane was prepared according to reported procedure,26,64 which was sandwiched between two graphite-felts. For full batteries, 50 mM cathode materials and 10 mM anode materials were dissolved in 0.5 M TBAPF₆-ACN (8 mL). The battery was galvanostatically charged/discharged at a current density of 2 mA cm⁻² within a potential range of 0-2.2 V.

Electrochemical impedance spectroscopy (EIS) of the RFBs before and after cycling was conducted on a Bio-Logic potentiostat under a frequency ranging from 200 kHz to 100 mHz and using a 10 mV AC amplitude signal.

Results and discussion

Molecular design and synthesis

A set of four compounds are synthesized for systematic investigation of PEGylation effects on battery performance in an organic solvent (Fig. 2a). Among the four compounds, PEG12-V and Me-V function as anolytes, and N-PEG12 phenothiazine (PEG12-PTZ) and C3-PTZ as catholytes (Fig. 2b). As the cathode redox material, compound PTZ undergoes one-electron oxidation to become a stable radical cation.82

Different pairings of the four electrolytes give four battery systems for thorough investigation. Instead of using KOH as the base for the deprotonation of PTZ to prepare C3-PTZ,79 a stronger base, sodium hydride, was used to afford a stronger PTZ nucleophile to react with PEG methyl ether tosylate (Scheme S1 and Fig. S1†), for the synthesis of compound PEG12-PTZ; 66% yield of PEG12-PTZ was obtained in high purity. The PEG12-PTZ compound is a purple liquid and is miscible with ACN in any proportion, to be compared to C3-PTZ as white crystal powders (Fig. S2†). The density of PEG12-V and PEG12-PTZ was 1.16 g mL⁻¹ and 1.17 g mL⁻¹, corresponding to a concentration of 0.79 M and 1.72 M, respectively. For twoelectron-active viologen, the electron concentration of PEG12-V is 1.58 M. The high solubility of PTZ is required to improve the energy density of the NAORFBs.

Electrochemical properties

The electrochemical properties of the electrolytes were characterized by CV in ACN with 0.1 M TBAPF₆ as the supporting electrolyte (Fig. 2c). The single-electron oxidation of PEG12-PTZ exhibits a reversible redox couple at 0.39 V vs. Ag/Ag⁺. The compound PEG12-V presents two redox peaks at -0.74 V and -1.15 V vs. Ag/Ag⁺. The pairing of **PEG12-V** and **PEG12-PTZ** gives

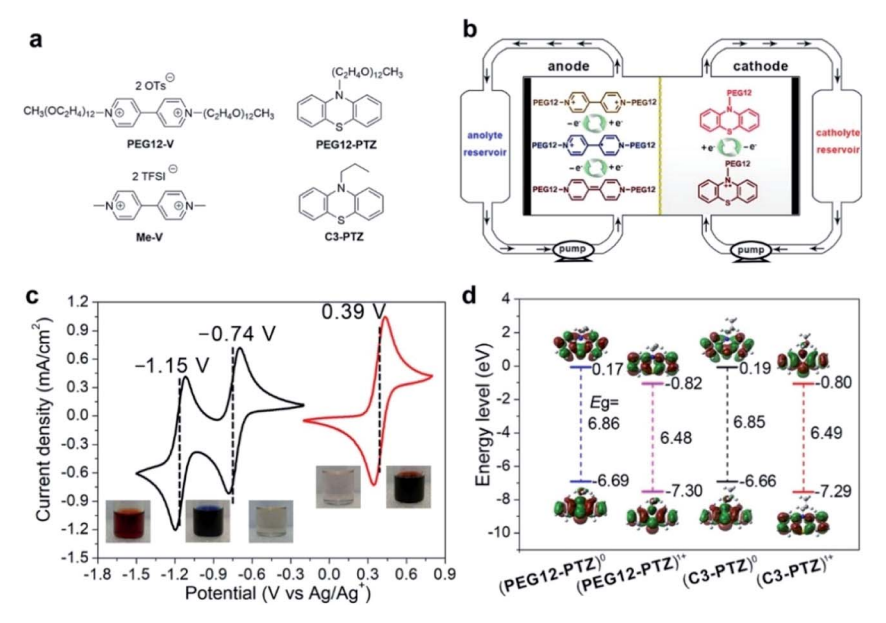


Fig. 2 (a) Molecular structures of compounds PEG12-V, Me-V, PEG12-PTZ, and C3-PTZ. (b) Redox reactions at the negative and positive sides during charge and discharge. (c) CV scans of PEG12-PTZ and PEG12-V (5.0 mM of both) in 0.1 M TBAPF₆-ACN on a glassy carbon electrode at a scan rate of 50 mV s⁻¹. (d) HOMO/LUMO of PEG12-PTZ and C3-PTZ on the redox-neutral and one-electron oxidized states.

a potential difference as high as 1.54 V. Moreover, the introduction of the PEG chain had negligible effect on the redox potential of the electroactive materials (Fig. S3†). Molecular Orbital (MO) Density Functional Theory (DFT) calculations for PEG12-PTZ and C3-PTZ in the two oxidation states were performed to evaluate the corresponding redox potentials during the electrochemical processes. The results show that for both C3-PTZ and PEG-PTZ, the HOMOs and LUMOs are almost identical and mapped through three PTZ rings symmetrically (Fig. 2d). Owing to the electron delocalization and conjugation, the HOMO orbitals show stable structures for C3-PTZ and **PEG12-PTZ.** The energy gaps (E_g) for the different redox states of C3-PTZ and PEG12-PTZ are almost identical, further confirming that the presence of the PEG unit does not affect the electrochemical properties. The E_g for the original oxidation state of both C3-PTZ and PEG12-PTZ is higher than that for the oneelectron oxidation state, indicating higher energy is needed for electron transfer in redox reactions. The crossover issue is one of the long-standing challenges in NAORFBs. 26,83 One of the advantages of PEGylation is that it can increase the molecular size of organic electroactive compounds and alleviate the crossover issue. A three-day permeability experiment was conducted by monitoring the concentration of active materials in the test chamber of a H-cell (Fig. S4†). Compound PEG12-PTZ presented a significant decreased crossover rate for the CANF membrane (1.31 \times 10⁻⁹ cm² s⁻¹), a tenth lower than that of C3-PTZ $(16.46 \times 10^{-9} \text{ cm}^2 \text{ s}^{-1}, \text{ Fig. S5}\dagger)$ owing to its bigger molecular size (Table 1). A similar trend was observed for viologens.64 It is worth noting that with similar molecular diameters (PEG12-PTZ vs. PEG12-V, and C3-PTZ vs. Me-V), viologens presented a lower permeability owing to their two positive charges and the Donnan exclusion of the CANF separator.64

To investigate the effect of PEGylation on the stability of PTZ, we repeated CV scans of PEG12-PTZ and C3-PTZ in 0.1 M TBAPF₆-ACN for 500 cycles. The overlapped traces showed the electrochemical stability of PEG12-PTZ in a non-aqueous electrolyte (Fig. S6a†). Meanwhile, C3-PTZ presented the same stability property (Fig. S6b†). In addition, the PTZ and viologen CV scans at different charge states showed that the redox potential and peak current density had almost no change after 5 days (Fig. S7†), which concluded that PEGylation did not affect their electrochemical stability.

The electrochemical kinetics of **PEG12-PTZ** in 0.1 M TBAPF₆–ACN were studied by the RDE method (Fig. 3a). The diffusion coefficient (D) of **PEG12-PTZ** was calculated from Levich plot (Fig. 3b), ^{46,48,80} which yielded a diffusion coefficient of 1.23 × 10^{-5} cm² s⁻¹, consistent with that from the Randle–Sevcik equation ($D_{\rm O}=1.10\times10^{-5}$ cm² s⁻¹ and $D_{\rm R}=9.88\times10^{-6}$ cm² s⁻¹) (Fig. S8 and Table S1†). The diffusion coefficient of **PEG12-PTZ** is slightly lower than that of **C3-PTZ** (1.61 × 10^{-5} cm² s⁻¹) (Fig. S9†), presumably owing to the increased viscosity from the PEG chains. Application of the Koutecký–Levich plot gave the

Table 1 Molecular sizes and permeability properties of the four compounds

Compound	Charge state ^b	Molecular diameter (nm)	Permeability $(\text{cm}^2 \text{ s}^{-1} \times 10^9)$
PEG12-PTZ	0	1.20	1.31
C3-PTZ	0	0.82	16.46
PEG12-V ^a	+2	1.43	0.35
Me-V ^a	+2	0.78	2.60

^a Data for **PEG12-V** and **Me-V** were derived from ref. 64. ^b The charge state refers to the viologen cations.

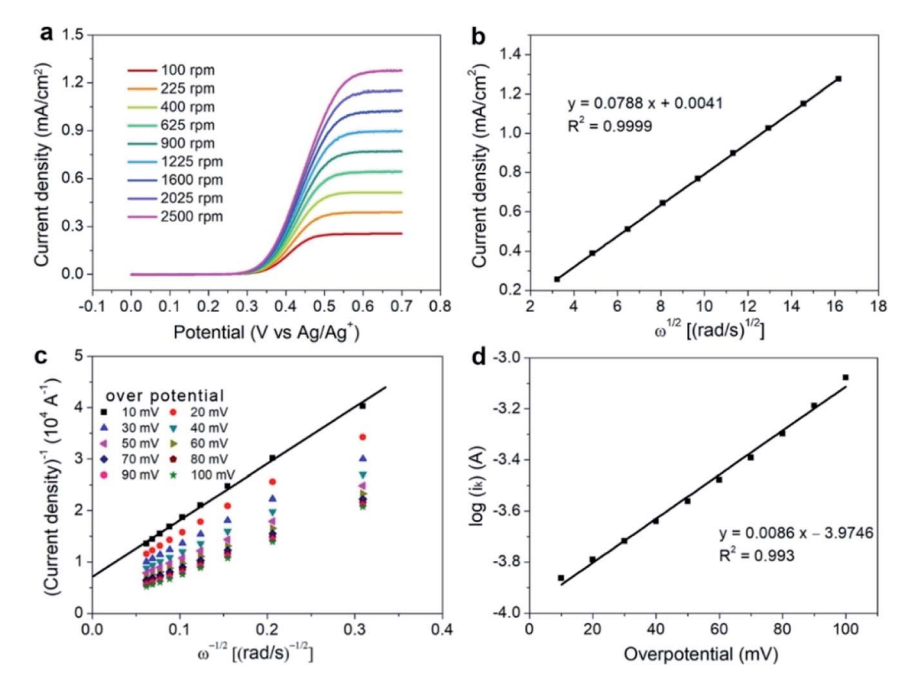


Fig. 3 (a) Linear sweep voltammetry of 1 mM of PEG12-PTZ in 0.1 M TBAPF₆-ACN at different rotation rates from 100 to 2500 rpm. (b) Levich plot from the obtained limiting currents. (c) Koutecký-Levich plot (i^{-1} vs. $\omega^{-1/2}$) of 1 mM of PEG-PTZ. (d) Plot of $\log(i_k)$ vs. overpotential.

mass-transfer-independent kinetic current i_k from the intercept of linear fitting (Fig. 3c). 20,62 The Butler-Volmer equation 41,62 via a Tafel plot yielded the exchange current i_0 , and then provided the kinetic oxidation rate constant k_0 ($k_0 = 5.64 \times 10^{-3} \text{ cm s}^{-1}$) *via* $i_0 = FAk_0C_0$ (Fig. 3d). The kinetic oxidation rate constant of C3-PTZ in 0.1 M TBAPF₆-ACN is 9.88×10^{-3} cm s⁻¹, slightly higher than that of PEG-PTZ, indicating that the introduction of PEG reduces the reaction rate constant of PTZ. However, the transfer coefficient (α) of C3-PTZ, obtained from the Tafel analysis, is only 0.315, which is lower than that of **PEG12-PTZ** (α = 0.492). The latter value is close to 0.5, which is the value for an ideally reversible redox reaction.62

Battery performance

The battery was assembled for rate performance and long cyclability tests using 50 mM PEG12-PTZ and 10 mM PEG12-V as catholyte and anolyte, respectively. The excess PEG12-PTZ was used to ensure the two-electron utilization of PEG12-V. The investigation of the all-PEGylated RFB was initiated with open circuit voltage (OCV) measurements at various states of charge (SOC) (Fig. S10†). The resulting all-PEGylated PEG12-PTZ/ PEG12-V battery presented an OCV increasing nearly linearly from 0.97 V at 5% SOC to 1.17 V at 45% SOC, and from 1.42 V at 50% SOC to 1.59 V at 95% SOC. The two charge platforms correspond to the two redox peaks of PEG12-V in CV scans. Similarly, the discharge plot showed two platforms. Additionally, the polarization voltage was as small as 75 mV, indicating the low internal impedance of the all-PEGylated PEG12-PTZ/ PEG12-V battery.

As the power density of a RFB is directly related to the rate property, a PEG12-PTZ/PEG12-V battery was galvanostatically

charged/discharged at different current densities from 1 to 5 mA cm² with an interval of 1 mA cm⁻² (Fig. 4a). At a current density of 1 mA cm⁻², the battery displayed a capacity of 5.03 mA h (93.4% of the theoretic capacity) with a coulombic efficiency of 97.7% and energy efficiency of 88.3%. With increased current density, the overpotential increases and discharge capacity decreases owing to the intrinsic internal impedance of the battery. However, even at a current density as high as 5 mA cm⁻² the battery still presented a discharge capacity of 4.19 mA h, corresponding to 78.2% of the theoretical capacity. It should be noted that the coulombic efficiency increased from 97.7% at 1 mA cm $^{-2}$ to 99.7% at 5 mA cm $^{-2}$ (Fig. 4b). The excellent rate performance was rooted in the high diffusion coefficient and kinetic oxidation rate constant of organic redox species in non-aqueous electrolytes.

Given that the coulombic efficiency of the battery is up to 99.0% at a current density of 2 mA cm⁻² (Fig. 4) and that the utilization of active materials exceeded 91.4%, the PEG12-PTZ/ PEG12-V battery was galvanostatically charged/discharged at a current density of 2 mA cm⁻² to investigate long cyclability. The battery possessed a capacity of 4.84 mA h with a capacity retention of 69.0% after 300 cycles (99.9% per cycle) (Fig. 5a) and an average coulombic efficiency of 99.7% (Fig. 5b). In addition, no evident change was observed for the charge/ discharge profiles at different cycle numbers (Fig. S11†), except for a slight reduction in capacity, exhibiting a stable energy efficiency of 72.7%. CV scans after 300 cycles indicated that the crossover of PEG12-PTZ through the CANF separator was negligible (Fig. 5c). EIS plots of the battery before and after the 300 cycles showed that there was a slight increase in the high-frequency impedance (Fig. 5d). However, the charge transfer impedance of the battery48 showed an evident decrease

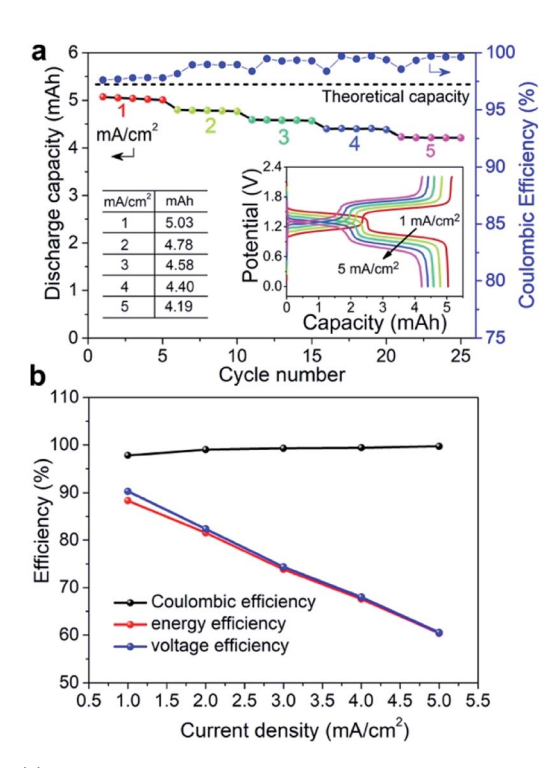


Fig. 4 (a) Discharge capacity and coulombic efficiency of the PEG12-PTZ/PEG12-V battery at varied current densities. Inset: charge/discharge profiles. (b) Average coulombic efficiency, energy efficiency, and voltage efficiency at different charge/discharge current densities.

presumably because of the prolonged soaking time of the CANF separator in the electrolyte. The stable impedance caused stable charge/discharge profiles and a long operating lifetime.

To investigate the structure-performance relationship, we studied the half-PEGylated batteries (C3-PTZ/PEG12-V and PEG12-PTZ/Me-V) and non-PEGylated battery (C3-PTZ/Me-V). The C3-PTZ/PEG12-V battery exhibited good capacity retention in the first 125 cycles (Fig. 5a), but with poor energy efficiency, especially after 100 cycles (Fig. 5b). The poor energy efficiency was attributed to the gradually increasing polarization during the charge/discharge process (Fig. S12a†). The redox peak for the catholyte C3-PTZ was observed in the anolyte side (Fig. S12b†) at almost the same current intensity as that of the same species in the catholyte, consistent with the permeability findings that C3-PTZ had a much higher permeability than PEG-V. The catholyte C3-PTZ may react with anolyte PEG12-V in the pores of the CANF membrane, resulting in increased internal resistance of the battery (Fig. S12c†). The PEG12-PTZ/Me-V and C3-PTZ/Me-V batteries displayed a stable energy efficiency but rapid capacity fading (Fig. 5a, b and S12d, g†). The same batteries also showed relatively low coulombic efficiency (Table 2) due to the serious crossover of Me-V and C3-PTZ, which was confirmed by the CV scans after battery cycling (Fig. S12e and h†). The PEG12-PTZ/Me-V and C3-PTZ/Me-V batteries were charged/discharged for 100 and 50 cycles, respectively. Despite the fewer cycle numbers compared to those in the all PEGylated (300 cycles) and C3-PTZ/PEG12-V (200 cycles) batteries, an evident internal impedance increase of both batteries was still

observed (Fig. S12f and i†). The increase of impedance was presumably owing to the precipitates formed from the reaction of **PTZ**s with viologens on the membranes during the charge/discharge processes.

Mechanistic analysis

The pre- and post-cycling anolyte and catholyte solutions of all the four batteries were analyzed by proton nuclear magnetic resonance (1H NMR, Fig. S13-S16†) and CV to elucidate the possible degradation mechanism. The analyte solutions were comprised of the analyte species (PEG12-V or Me-V) and various amounts of catholyte species from the crossover; no additional ¹H NMR signals were observed, indicating that both the anolyte and catholyte species were electrochemically stable in the anolyte chamber. By contrast, besides the anolyte species from the crossover, unexpected proton signals (panels (a) in Fig. S13-S16†) were detected in the catholyte chamber, suggesting that side reactions occurred in the electrochemically oxidizing catholyte chamber. We hypothesized three possible side reactions: (A) the catholyte molecules (PEG12-PTZ and C3-PTZ) underwent oxidative decomposition during the charging process; (B) viologen compounds crossed from the analyte side, decomposing under the oxidizing conditions in the catholyte chamber; and (C) the reduced viologens (radical anion) reacted with oxidized PTZs (radical cation) in the catholyte chamber to form a new chemical species, rather than returning to their neutral, original states. Extensive experiments were conducted to confirm or eliminate the hypotheses. (1) CV scans of PTZs for repetitive 500 cycles (Fig. S6†) indicated that the pure PTZs were electrochemically stable for single-electron oxidation, thus eliminating hypothesis A. (2) Repetitive CV scans of PEG12-V in different potential ranges were conducted. Though the interconversion between PEG12-V and its radical anion is reversible (Fig. S17†) from -1.5 to -0.2 V vs. Ag/Ag⁺, an evident current decrease was observed in the more positive scan range (from -1.5 to 0.8 V vs. Ag/Ag⁺), indicating the instability of **PEG12-V** under oxidizing conditions, which supports hypothesis B. (3) Separate electrolysis of PEG12-PTZ and PEG12-V formed their corresponding radical anion and radical cation, respectively, and then the two radical species were mixed in a stoichiometric ratio. The ¹H NMR spectrum of the resultant solution is the sum of the spectra of PEG12-V and PEG12-PTZ (Fig. S18†), suggesting neat redox neutralization of the two radicals without forming side products. This experiment result is against hypothesis C. Overall, the stability issue of viologen molecules under oxidizing conditions is a possible cause of battery degradation. The mechanistic analysis here not only provides an explanation for the battery capacity decay, but also emphasizes the importance of addressing the crossover issue by designing the next generation of redox-active molecules and suited membrane separators.

Concentration dependence

The PEG12-PTZ/PEG12-V batteries with higher concentrations were investigated to pursuit higher energy density. The battery

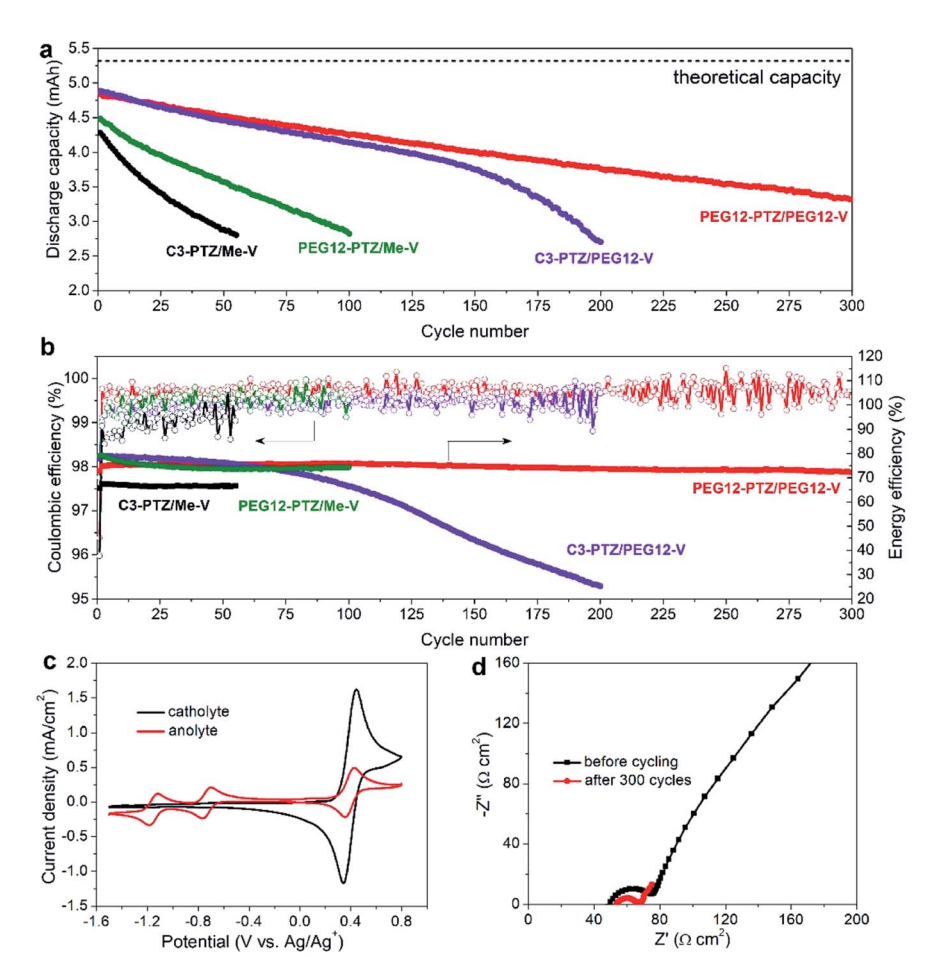


Fig. 5 (a) Discharge capacity vs. cycle number of the PEG12-PTZ/PEG12-V (red), C3-PTZ/PEG12-V (violet), PEG12-PTZ/Me-V (green), and C3-PTZ/Me-V (black) batteries. (b) Coulombic and energy efficiencies vs. cycle number. (c) CV scans of catholyte and anolyte for PEG12-PTZ/ PEG12-V battery after 300 cycles. (d) AC impedance spectra of PEG12-PTZ/PEG12-V battery before cycling and after 300 cycles.

was initially assembled with 480 mM PEG12-PTZ and 200 mM PEG12-V mix electrolytes using a macroporous Daramic membrane as the separator. Before cycling, the battery displayed an impedance of 17.5 Ω cm⁻² (Fig. 6a). The battery was galvanostatically charged/discharged at a current density of 20 mA cm⁻² and presented undesirable polarization and low coulombic efficiency (55%, Fig. 6b). Then electrolytes were diluted to $\frac{3}{4}$ and afforded 360 mM PEG12-PTZ and 150 mM PEG12-V mix electrolytes. Both impedance and polarization of the battery reduced with the decreased concentration with a coulombic efficiency of 72%. Different concentrations of electrolytes impose different viscosity effects on battery impedance; the higher electrolyte concentration, the more

viscous the electrolyte solution is; therefore, batteries with higher electrolyte concentration present higher impedance. After further diluted to concentrations of 240 mM PEG12-PTZ and 100 mM PEG12-V, the battery presented a stable coulombic efficiency of 92% (Fig. 6c). The gradual decay of energy and voltage efficiencies were observed during cycling. CV scans of the post-cycling electrolyte indicated current density decrease for anolyte presumably due to the interaction of PEG12-PTZ and the reduced viologen species. The concentration-dependence study suggests that the high viscosity of PEG units and the possible side reaction of the anolytes and catholytes could be the two barriers to enhancing the energy density.

Table 2 Average coulombic efficiency and capacity retention of the four batteries

Battery	Average coulombic efficiency (%)	Capacity retention per cycle (%)	Overall capacity retention
PEG12-PTZ/PEG12-V	99.71	99.90	68.6% after 300 cycles
C3-PTZ/PEG12-V	99.41	99.78	55.3% after 200 cycles
PEG12-PTZ/Me-V	99.48	99.63	62.9% after 100 cycles
C3-PTZ/Me-V	98.99	99.37	65.4% after 50 cycles

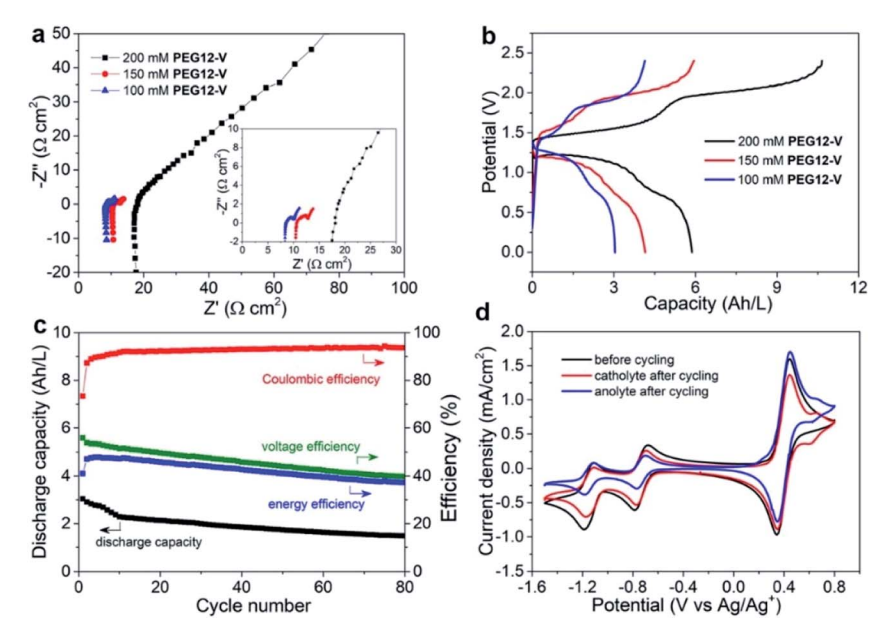


Fig. 6 (a) EIS of the PEG12-PTZ/PEG12-V batteries at different concentrations. (b) First charge/discharge curves. (c) Discharge capacity and efficiencies of battery with 240 mM PEG12-PTZ and 100 mM PEG12-V mix electrolytes. (d) CV scans of catholyte and anolyte after cycling and mix electrolyte before cycling.

Conclusions

In summary, this study demonstrated that PEGylation of organic redox-active materials is a promising strategy to enhance the performance of NAORFBs by increasing the molecular size of compounds without sacrificing their electrochemical properties and alleviating the permeability of active materials in catholyte and anolyte for long cyclability. Combined with the CANF separator, the all-PEGylated battery (PEG12-PTZ and PEG12-V) delivered an excellent capacity retention of 99.9% per cycle and an average coulombic efficiency of 99.7% after 300 charge/discharge cycles. The half-PEGylated (C3-PTZ/PEG12-V and PEG12-PTZ/Me-V) and non-PEGylated (C3-PTZ/Me-V) batteries were also investigated for structure-function relationship and mechanistic studies, and the instability of viologen molecules under oxidizing conditions was presented. This work highlights the importance of molecular engineering in NAORFBs and opens a new avenue for utilizing the PEGylation strategy in future redox flow battery technology.

Conflicts of interest

There are no conflicts to declare.

Acknowledgements

The authors acknowledge the University of Cincinnati for startup funding support, and Ohio Supercomputer Center for providing the computational resources. NMR experiments were performed on a Bruker AVANCE NEO 400 MHz NMR spectrometer funded by NSF-MRI grant CHE-1726092.

Notes and references

- 1 Z. P. Li, L. Wang, R. R. Liu, Y. P. Fan, H. G. Meng, Z. P. Shao, G. L. Cui and S. P. Pang, *Adv. Energy Mater.*, 2019, **9**, 1902142.
- 2 Z. P. Shao, Z. W. Wang, Z. P. Li, Y. P. Fan, H. G. Meng, R. R. Liu, Y. Wang, A. Hagfeldt, G. L. Cui and S. P. Pang, *Angew. Chem., Int. Ed.*, 2019, 58, 5587–5591.
- 3 Q. Jiang, Y. Zhao, X. W. Zhang, X. L. Yang, Y. Chen, Z. M. Chu, Q. F. Ye, X. X. Li, Z. G. Yin and J. B. You, *Nat. Photonics*, 2019, 13, 460–466.
- 4 Q. L. Wang, H. R. Zhang, Z. L. Cui, Q. Zhou, X. H. Shangguan, S. W. Tian, X. H. Zhou and G. L. Cui, *Energy Storage Materials*, 2019, 23, 466–490.
- 5 G. Xu, X. Shangguan, S. Dong, X. Zhou and G. Cui, *Angew. Chem., Int. Ed.*, 2020, **59**, 3400–3415.
- 6 Q. Zhou, J. Ma, S. Dong, X. Li and G. Cui, Adv. Mater., 2019, 31, 1902029.
- 7 Y. Lu, L. Yu and X. W. D. Lou, Chem, 2018, 4, 972-996.
- 8 K. Liang, K. Marcus, S. Zhang, L. Zhou, Y. Li, S. T. De Oliveira, N. Orlovskaya, Y. H. Sohn and Y. Yang, *Adv. Energy Mater.*, 2017, 7, 1701309.
- 9 L. Wang, K. Liang, G. Wang and Y. Yang, *J. Mater. Chem. A*, 2018, **6**, 13968–13974.
- 10 Y. Yang, Y. Zhong, Q. Shi, Z. Wang, K. Sun and H. Wang, Angew. Chem., Int. Ed., 2018, 130, 15775–15778.
- 11 Y. Zhong, L. Yin, P. He, W. Liu, Z. Wu and H. Wang, *J. Am. Chem. Soc.*, 2018, **140**, 1455–1459.
- 12 Q. Shi, Y. Zhong, M. Wu, H. Wang and H. Wang, *Proc. Natl. Acad. Sci. U. S. A.*, 2018, **115**, 5676–5680.
- 13 P. He, Y. Fang, X. Y. Yu and X. W. Lou, *Angew. Chem., Int. Ed.*, 2017, **56**, 12202–12205.

Paper

- 14 Z. Xu, F. Xie, J. Wang, H. Au, M. Tebyetekerwa, Z. Y. Guo, S. Y. Yang, Y. S. Hu and M. M. Titirici, *Adv. Funct. Mater.*, 2019, 29, 1903895.
- 15 K. Liang, L. Ju, S. Koul, A. Kushima and Y. Yang, Adv. Energy Mater., 2019, 9, 1802543.
- 16 A. B. Du, H. R. Zhang, Z. H. Zhang, J. W. Zhao, Z. L. Cui, Y. M. Zhao, S. M. Dong, L. L. Wang, X. H. Zhou and G. L. Cui, Adv. Mater., 2019, 31, 1805930.
- 17 A. B. Du, Z. H. Zhang, H. T. Qu, Z. L. Cui, L. X. Qiao, L. L. Wang, J. C. Chai, T. Lu, S. M. Dong, T. T. Dong, H. M. Xu, X. H. Zhou and G. L. Cui, *Energy Environ. Sci.*, 2017, 10, 2616–2625.
- 18 B. H. Hu, J. L. Luo, M. Hu, B. Y. Yuan and T. L. Liu, Angew. Chem., Int. Ed., 2019, 58, 16629–16636.
- 19 T. Liu, X. Wei, Z. Nie, V. Sprenkle and W. Wang, *Adv. Energy Mater.*, 2016, **6**, 1501449.
- 20 Z. J. Yang, L. C. Tong, D. P. Tabor, E. S. Beh, M. A. Goulet, D. De Porcellinis, A. Aspuru-Guzik, R. G. Gordon and M. J. Aziz, Adv. Energy Mater., 2018, 8, 1702056.
- 21 X. Wei, W. Pan, W. Duan, A. Hollas, Z. Yang, B. Li, Z. Nie, J. Liu, D. Reed, W. Wang and V. Sprenkle, *ACS Energy Lett.*, 2017, 2, 2187–2204.
- 22 M. Burgess, J. S. Moore and J. Rodríguez-López, *Acc. Chem. Res.*, 2016, **49**, 2649–2657.
- 23 M. J. Baran, M. N. Braten, E. C. Montoto, Z. T. Gossage, L. Ma, E. Chénard, J. S. Moore, J. Rodríguez-López and B. A. Helms, *Chem. Mater.*, 2018, 30, 3861–3866.
- 24 G. Nagarjuna, J. Hui, K. J. Cheng, T. Lichtenstein, M. Shen, J. S. Moore and J. Rodríguez-López, *J. Am. Chem. Soc.*, 2014, **136**, 16309–16316.
- 25 J. Yu, Y. S. Hu, F. Pan, Z. Zhang, Q. Wang, H. Li, X. Huang and L. Chen, *Nat. Commun.*, 2017, **8**, 14629.
- 26 S. O. Tung, S. L. Fisher, N. A. Kotov and L. T. Thompson, *Nat. Commun.*, 2018, 9, 4193.
- 27 C. Jia, F. Pan, Y. G. Zhu, Q. Huang, L. Lu and Q. Wang, *Sci. Adv.*, 2015, 1, e1500886.
- 28 F. R. Brushett, J. T. Vaughey and A. N. Jansen, *Adv. Energy Mater.*, 2012, 2, 1390–1396.
- 29 Y. Ding, Y. Zhao, Y. Li, J. B. Goodenough and G. Y. Yu, *Energy Environ. Sci.*, 2017, **10**, 491–497.
- 30 B. Hu and T. L. Liu, J. Energy Chem., 2018, 27, 1326–1332.
- 31 G. Kwon, S. Lee, J. Hwang, H. S. Shim, B. Lee, M. H. Lee, Y. Ko, S. K. Jung, K. Ku, J. Hong and K. Kang, *Joule*, 2018, 2, 1771–1782.
- 32 Q. Liu, A. E. S. Sleightholme, A. A. Shinkle, Y. Li and L. T. Thompson, *Electrochem. Commun.*, 2009, **11**, 2312–2315.
- 33 Y. Ding, C. Zhang, L. Zhang, H. Wei, Y. Li and G. Yu, *ACS Energy Lett.*, 2018, 3, 2641–2648.
- 34 C. Zhang, Z. Niu, Y. Ding, L. Zhang, Y. Zhou, X. Guo, X. Zhang, Y. Zhao and G. Yu, Chem, 2018, 4, 2814–2825.
- 35 T. Ma, Z. Pan, L. Miao, C. Chen, M. Han, Z. Shang and J. Chen, *Angew. Chem., Int. Ed.*, 2018, 57, 3158–3162.
- 36 K. Gong, Q. Fang, S. Gu, S. F. Y. Li and Y. Yan, *Energy Environ. Sci.*, 2015, **8**, 3515–3530.
- 37 X. Wei, W. Xu, M. Vijayakumar, L. Cosimbescu, T. Liu, V. Sprenkle and W. Wang, *Adv. Mater.*, 2014, 26, 7649–7653.

- 38 X. Wei, L. Cosimbescu, W. Xu, J. Z. Hu, M. Vijayakumar, J. Feng, M. Y. Hu, X. Deng, J. Xiao, J. Liu, V. Sprenkle and W. Wang, Adv. Energy Mater., 2015, 5, 1400678.
- 39 X. Wei, W. Duan, J. Huang, L. Zhang, B. Li, D. Reed, W. Xu, V. Sprenkle and W. Wang, *ACS Energy Lett.*, 2016, 1, 705–711.
- 40 X. Wei, W. Xu, J. Huang, L. Zhang, E. Walter, C. Lawrence, M. Vijayakumar, W. A. Henderson, T. Liu, L. Cosimbescu, B. Li, V. Sprenkle and W. Wang, *Angew. Chem., Int. Ed.*, 2015, 54, 8684–8687.
- 41 B. Huskinson, M. P. Marshak, C. Suh, S. Er, M. R. Gerhardt, C. J. Galvin, X. Chen, A. Aspuru-Guzik, R. G. Gordon and M. J. Aziz, *Nature*, 2014, 505, 195–198.
- 42 K. Lin, Q. Chen, M. R. Gerhardt, L. Tong, S. B. Kim, L. Eisenach, A. W. Valle, D. Hardee, R. G. Gordon and M. J. Aziz, *Science*, 2015, 349, 1529–1532.
- 43 A. Hollas, X. Wei, V. Murugesan, Z. Nie, B. Li, D. Reed, J. Liu, V. Sprenkle and W. Wang, *Nat. Energy*, 2018, 3, 508–514.
- 44 C. Zhang, Z. Niu, S. Peng, Y. Ding, L. Zhang, X. Guo, Y. Zhao and G. Yu, *Adv. Mater.*, 2019, **31**, 1901052.
- 45 D. G. Kwabi, K. Lin, Y. Ji, E. F. Kerr, M.-A. Goulet, D. De Porcellinis, D. P. Tabor, D. A. Pollack, A. Aspuru Guzik, R. G. Gordon and M. J. Aziz, *Joule*, 2018, 2, 1894–1906.
- 46 K. Lin, R. Gómez-Bombarelli, E. S. Beh, L. Tong, Q. Chen, A. Valle, A. Aspuru-Guzik, M. J. Aziz and R. G. Gordon, *Nat. Energy*, 2016, 1, 16102.
- 47 R. F. Service, Science, 2018, 362, 508-509.
- 48 B. Hu, C. DeBruler, Z. Rhodes and T. L. Liu, *J. Am. Chem. Soc.*, 2017, **139**, 1207–1214.
- 49 C. DeBruler, B. Hu, J. Moss, X. Liu, J. Luo, Y. Sun and T. L. Liu, *Chem*, 2017, 3, 961–978.
- 50 Z. G. Yang, J. L. Zhang, M. C. W. Kintner-Meyer, X. C. Lu, D. W. Choi, J. P. Lemmon and J. Liu, *Chem. Rev.*, 2011, 111, 3577–3613.
- 51 A. A. Shinkle, T. J. Pomaville, A. E. S. Sleightholme, L. T. Thompson and C. W. Monroe, *J. Power Sources*, 2014, 248, 1299–1305.
- 52 H. Liang, X. Qiu, S. Zhang, W. Zhu and L. Chen, *J. Appl. Electrochem.*, 2004, 34, 1211–1214.
- 53 L. Su, R. M. Darling, K. G. Gallagher, W. Xie, J. L. Thelen, A. F. Badel, J. L. Barton, K. J. Cheng, N. P. Balsara, J. S. Moore and F. R. Brushett, J. Electrochem. Soc., 2016, 163, A5253–A5262.
- 54 I. L. Escalante-García, J. S. Wainright, L. T. Thompson and R. F. Savinell, *J. Electrochem. Soc.*, 2015, **162**, A363–A372.
- 55 J. Huang, Z. Yang, M. Vijayakumar, W. Duan, A. Hollas, B. Pan, W. Wang, X. Wei and L. Zhang, *Adv. Sustainable Syst.*, 2018, 2, 1700131.
- 56 J. D. Milshtein, S. L. Fisher, T. M. Breault, L. T. Thompson and F. R. Brushett, *ChemSusChem*, 2017, **10**, 2080–2088.
- 57 N. H. Attanayake, J. A. Kowalski, K. V. Greco, M. D. Casselman, J. D. Milshtein, S. J. Chapman, S. R. Parkin, F. R. Brushett and S. A. Odom, *Chem. Mater.*, 2019, 31, 4353–4363.
- 58 J. Huang, L. Cheng, R. S. Assary, P. Wang, Z. Xue, A. K. Burrell, L. A. Curtiss and L. Zhang, *Adv. Energy Mater.*, 2015, 5, 1401782.

- 59 J. D. Saraidaridis and C. W. Monroe, *J. Power Sources*, 2019, 412, 384–390.
- 60 C. Zhang, Y. Qian, Y. Ding, L. Zhang, X. Guo, Y. Zhao and G. Yu, Angew. Chem., Int. Ed., 2019, 131, 119–7124.
- 61 Y. Ding, Y. Li and G. Yu, Chem, 2016, 1, 790-801.
- 62 T. Janoschka, N. Martin, U. Martin, C. Friebe, S. Morgenstern, H. Hiller, M. D. Hager and U. S. Schubert, *Nature*, 2015, **527**, 78–81.
- 63 M. Burgess, E. Chénard, K. Hernández-Burgos, G. Nagarjuna, R. S. Assary, J. Hui, J. S. Moore and J. Rodríguez-López, *Chem. Mater.*, 2016, 28, 7362–7374.
- 64 J. Chai, A. Lashgari, Z. Cao, C. K. Williams, X. Wang, J. Dong and J. Jiang, *ACS Appl. Mater. Interfaces*, 2020, DOI: 10.1021/acsami.0c01045.
- 65 W. Wang, W. Xu, L. Cosimbescu, D. Choi, L. Li and Z. Yang, *Chem. Commun.*, 2012, **48**, 6669–6671.
- 66 S. Maurya, S. H. Shin, K. W. Sung and S. H. Moon, *J. Power Sources*, 2014, **255**, 325–334.
- 67 S. G. Robinson, Y. Yan, K. H. Hendriks, M. S. Sanford and M. S. Sigman, J. Am. Chem. Soc., 2019, 141, 10171–10176.
- 68 Y. Yan, S. G. Robinson, M. S. Sigman and M. S. Sanford, *J. Am. Chem. Soc.*, 2019, **141**, 15301–15306.
- 69 M. Sanford, A. Shrestha, K. Hendriks, M. Sigman and S. Minteer, *Chem.-Eur. J.*, 2020, DOI: 10.1002/ chem.202000749.
- 70 R. Darling, K. Gallagher, W. Xie, L. Su and F. Brushett, J. Electrochem. Soc., 2016, 163, A5029–A5040.
- 71 J. Luo, W. Wu, C. R. DeBruler, B. Hu, M. Hu and T. Liu, J. Mater. Chem. A, 2019, 7, 9130–9136.

- 72 J. Luo, B. Hu, C. Debruler, Y. Bi, Y. Zhao, B. Yuan, M. Hu, W. Wu and T. L. Liu, *Joule*, 2019, 3, 149–163.
- 73 B. Hwang, M. S. Park and K. Kim, *ChemSusChem*, 2015, 8, 310-314.
- 74 K. M. Roberts, M. A. Flahive and J. E. House, *Polyhedron*, 2013, 53, 240–242.
- 75 L. Cosimbescu, X. Wei, M. Vijayakumar, W. Xu, M. L. Helm, S. D. Burton, C. M. Sorensen, J. Liu, V. Sprenkle and W. Wang, Sci. Rep., 2015, 5, 14117.
- 76 J. A. Kowalski, M. D. Casselman, A. P. Kaur, J. D. Milshtein, C. F. Elliott, S. Modekrutti, N. H. Attanayake, N. Zhang, S. R. Parkin, C. Risko, F. R. Brushett and S. A. Odom, *J. Mater. Chem. A*, 2017, 5, 24371–24379.
- 77 J. D. Milshtein, A. P. Kaur, M. D. Casselman, J. A. Kowalski, S. Modekrutti, P. L. Zhang, N. Harsha Attanayake, C. F. Elliott, S. R. Parkin, C. Risko, F. R. Brushett and S. A. Odom, *Energy Environ. Sci.*, 2016, 9, 3531–3543.
- 78 L. Yang, G. Lin, D. Liu, K. J. Dria, J. Telser and L. Li, *J. Am. Chem. Soc.*, 2011, **133**, 10434–10447.
- 79 S. Ergun, C. F. Elliott, A. P. Kaur, S. R. Parkin and S. A. Odom, Chem. Commun., 2014, 50, 5339–5341.
- 80 E. S. Beh, D. De Porcellinis, R. L. Gracia, K. T. Xia, R. G. Gordon and M. J. Aziz, *ACS Energy Lett.*, 2017, 2, 639–644.
- 81 M. J. Frisch, G. Trucks, H. Schlegel, et al., Gaussian 09, Gaussian, Inc., Wallingford, CT, 2009.
- 82 A. P. Kaur, N. E. Holubowitch, S. Ergun, C. F. Elliott and S. A. Odom, *Energy Technol.*, 2015, 3, 476–480.
- 83 Y. Ding, C. Zhang, L. Zhang, Y. Zhou and G. Yu, *Chem. Soc. Rev.*, 2018, 47, 69–103.